

# PHYSICAL REVIEW D

## PARTICLES AND FIELDS

THIRD SERIES, VOLUME 41, NUMBER 3

1 FEBRUARY 1990

### Analyzing power for $\pi^- p$ charge exchange in the backward hemisphere from 301 to 625 MeV/c and a test of $\pi N$ partial-wave analyses

G. J. Kim\*

*Department of Physics, University of California at Los Angeles, Los Angeles, California 90024*

J. Arends<sup>†</sup>

*Department of Physics, University of California at Los Angeles, Los Angeles, California 90024  
and Department of Physics, Catholic University of America, Washington, D.C. 20064*

W. J. Briscoe

*Department of Physics, The George Washington University, Washington, D.C. 20052*

J. Engelage<sup>‡</sup> and B. M. K. Nefkens

*Department of Physics, University of California at Los Angeles, Los Angeles, California 90024*

M. E. Sadler

*Department of Physics, Abilene Christian University, Abilene, Texas 79699*

M. Taragin

*Department of Physics, The George Washington University, Washington, D.C. 20052*

H. J. Ziock<sup>§</sup>

*Department of Physics, University of California at Los Angeles, Los Angeles, California 90024*

(Received 9 June 1989)

The analyzing power of  $\pi^- p \rightarrow \pi^0 n$  has been measured for  $p_\pi = 301$ –625 MeV/c with a transversely polarized target, mainly in the backward hemisphere. The final-state neutron and a  $\gamma$  from the  $\pi^0$  were detected in coincidence with two counter arrays. Our results are compared with predictions of recent  $\pi N$  partial-wave analyses by the groups of Karlsruhe-Helsinki, Carnegie-Mellon University–Lawrence Berkeley Laboratory (CMU-LBL), and Virginia Polytechnic Institute (VPI). At the lower incident energies little difference is seen among the three analyses, and there is excellent agreement with our data. At 547 MeV/c and above, our data strongly favor the VPI phases, and disagree with Karlsruhe-Helsinki and CMU-LBL analyses, which are the source of the  $\pi N$  resonance parameters given in the Particle Data Group table.

#### I. INTRODUCTION

The 1988 compilation by the Particle Data Group<sup>1</sup> lists 23 bona fide  $\pi N$  resonances—states which have been awarded three or four stars—and 17 candidate resonances with only one or two stars. The properties of each resonance, the mass, width, and elasticity, are all derived from  $\pi N$  partial-wave analyses (PWAs). It is important to have a complete and reliable listing of  $\pi N$  resonances and their properties to use in tests of quark models<sup>2–7</sup> and in Skyrmin-type calculations.<sup>8,9</sup> Thus, it is necessary to determine which of the PWAs is the most accurate.

There are currently three  $\pi N$  PWAs in active use. These have been obtained by the groups from Karlsruhe University–Helsinki University<sup>10</sup> (KH), Carnegie-Mellon University–Lawrence Berkeley Laboratory<sup>11</sup> (CL), and Virginia Polytechnic Institute and State University<sup>12</sup> (VPI). The characteristics of the resonances accessible at LAMPF as determined by these PWAs are listed in Table I. The traditional PWA technique used by all groups consists of data amalgamation, interpolation, and single-energy analyses as discussed in our preliminary report.<sup>13</sup> The main differences among the analyses are in the data base and the application of theoretical constraints. The VPI data base has been carefully pruned and frequently

TABLE I. The resonance pole position and the mass, width, and elasticity from KH, CL, and VPI PWAs of the  $\pi N$  states accessible at LAMPF.

	Re $W$ (MeV)	-Im $W$ (MeV)	$M$ (MeV)	$\Gamma$ (MeV)	$\eta$	PWA
$P_{33}(1232)$	1212	51				VPI
	1210	50	1232	120	1.0	CL
			1233	116	1.0	KH
$P_{11}(1440)$	1358 (I)	98				VPI
	1415 (II)	93				VPI
	1375	90	1440	340	0.68	CL
$D_{13}(1520)$	1509	62	1410	135	0.51	KH
	1510	57	1525	120	0.58	CL
			1519	114	0.54	KH
$S_{11}(1535)$	1449	86				VPI
	1510	130	1550	240	0.50	CL
			1526	120	0.38	KH

updated, but the KH and CL data bases are already 9 years old. The theoretical constraints are used to eliminate the ambiguities inherent in PWAs. To arrive at a unique solution, KH and CL use the trustworthy, albeit complicated, constraints from dispersion relations, whereas VPI uses an empirical ansatz with adjustable parameters. Also, VPI cuts off the analysis at 1.2 GeV/ $c$ .

For the last several years the VPI PWA has featured a  $P_{11}$  amplitude with two nearby poles in the region of the Roper resonance, something not appearing in other waves and avoided by the other two PWAs. The double pole has generated much speculation. For instance, Cutkosky<sup>14</sup> has emphasized the importance of the opening of the strong  $\pi\Delta$  channel close to the Roper mass, but it is surprising that the  $S_{11}$  with its large inelastic channel does not show a similar double pole. Less likely is the possibility that the double pole is an unforeseen consequence of the VPI parametrization. Thus, one is led to worry about exotic possibilities such as manifestation of a hybrid state consisting of three quarks and a gluon,<sup>15,16</sup> the  $\pi\Delta$  effect,<sup>17</sup> or perhaps even a  $q^4\bar{q}$  state.<sup>18</sup> We have investigated how best to differentiate between the three PWAs and have found that the analyzing power,  $A_N$ , measured using a transversely polarized target in  $\pi^-p \rightarrow \pi^0n$  [charge exchange (CEX)] in the backward direction to be the most sensitive way.

The original motivation for the experiment was the first measurement in this energy region of  $A_N(\pi^-p \rightarrow \gamma n)$ ; the reaction  $\pi^-p \rightarrow \gamma n$  will be referred to as REX (radiative exchange). Because the REX cross section is some 30–100 times smaller than the polarization-dependent CEX background, a clean REX-from-CEX separation was vital. We used a large counter setup that exploited the geometry of the two-body REX final state, resulting in excellent REX/CEX separation. Thus, along with REX results<sup>19</sup> we obtained a clean CEX sample with a statistical accuracy of an order of magnitude better than the existing data. We report here the experimental details, results, and conclusions from a measurement of  $A_N(\pi^-p \rightarrow \pi^0n)$  mainly in the backward direction at seven pion momenta from 301 to 625 MeV/ $c$ .

This momentum region includes the onset of the Roper resonance.

## II. EXPERIMENT

The experiment was performed in the East cave of the Pion and Particle Physics ( $P^3$ ) channel at the Clinton P. Anderson Meson Physics Facility (LAMPF) of the Los Alamos National Laboratory. The setup is shown in Fig. 1. The major components are a polarized-proton target,

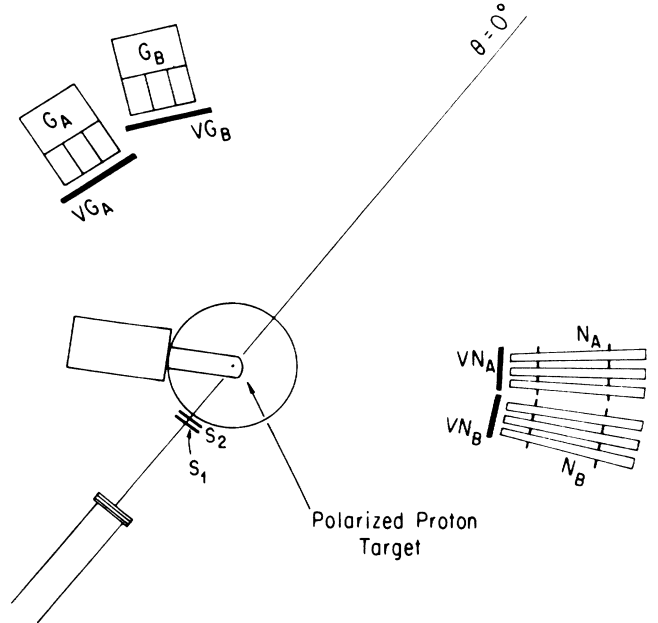


FIG. 1. Schematic of the experimental setup.  $S_1$  and  $S_2$  are the beam defining scintillation counters (not to scale).  $N_A$  and  $N_B$  are two sets of 15 element neutron detectors, and  $G_A$  and  $G_B$  are two sets of the corresponding 15 element  $\gamma$  detectors.  $VN_A$  and  $VN_B$  are charged-particle veto counters in front of the neutron detectors, and  $VG_A$  and  $VG_B$  are veto counters for the  $\gamma$  detectors. The  $0^\circ$  line is used for reference. The actual pion beam is bent by the magnetic field of the polarized proton target.

two independent sets of neutron and  $\gamma$  detectors, and beam-control and -monitoring devices. Not shown in the figure is the extensive shielding arrangement. Concrete blocks were stacked to form a cave around the neutron detectors to reduce the background from backscattering and skyshine; the blocks were lined with 2.5-cm-thick polyethylene sheets for extra neutron shielding.

### A. Pion beams

A summary of the beam characteristics is given in Table II. The beam was defined by a pair of thin scintillation counters  $S1$  and  $S2$  located 60 cm upstream of the target. The coincidence between  $S1$  and  $S2$  was the basis for the beam rate listed in Table II. Decay muon telescopes consisting of a pair of small counters were installed, one above and another below the beam pipe, for checking muons from pions decaying in flight; they were used as a relative beam monitor. A beam-profile monitor (BPM) consisting of a  $13 \times 13$ -cm<sup>2</sup> multiwire proportional chamber (MWPC) with a sequential wire-readout system was permanently installed in the beam; the  $X$  and  $Y$  oscilloscope display of the beam profile provided visual monitoring. The beam spot at the target was approximately 2 cm in diameter as measured with polaroid film placed against the target. The central beam momentum of the  $P^3$  channel is known to  $\pm 0.3\%$  (Ref. 20).

The angular definition of the  $\gamma$ - and neutron-detector position was complicated by the bending of the incident beam in the 25-kG field of the target magnet. The direction of the magnetic field pointed down throughout the experiment and caused the negative pion beams to be deflected to the right on passing through the target, see Fig. 2. Since the magnitude of the bending depends on the momentum of the beam, it is convenient to measure all laboratory angles with respect to the undeflected beam line ( $0^\circ$  in Fig. 2). The angle of the beam at the point of interaction in the target is called the incident beam angle  $\theta_{inc}$ . The central  $\theta_{inc}$  ranged from  $13.4^\circ$  for the 625-MeV/ $c$  beam to  $27.4^\circ$  for the 301-MeV/ $c$  beam, see Table II. Depending on the interaction point in the 4.6-cm-diameter target, the incident angle can vary as much as  $\pm 2^\circ$  from the central value. The central incident beam angle was calculated by tracing the trajectory of the beam starting from about 2 m upstream of the target to the center of the target. A small horizontal steering magnet

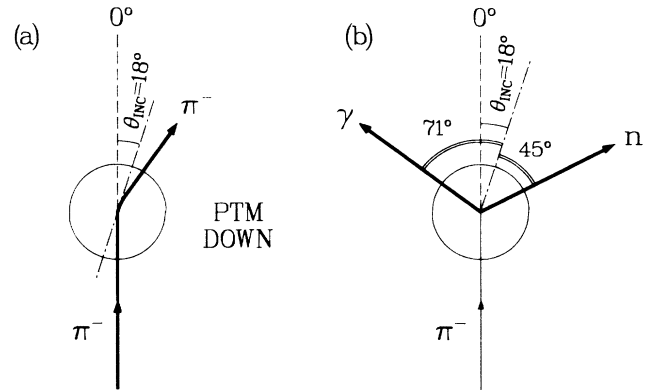


FIG. 2. (a) Schematic representation of the trajectory of the 471-MeV/ $c$  negative pion beam in the 25-kG field of the target magnet. (b) Laboratory production angle of the REX  $\gamma$  and neutron for 471-MeV/ $c$  pions at  $90^\circ$  c.m.

located 4.5 m upstream of the target was used to steer the beam on target.

### B. Polarized proton target

The target material was ethylene glycol [ $C_2H_2(OH)_2$ ], except for the 301- and 316-MeV/ $c$  data runs in which 1,2-propanediol [ $C_3H_6(OH)_2$ ] was used. The target was prepared in the form of beads about 1 mm in diameter. The beads were loaded into a 40-cm<sup>2</sup> spherical cell, which was flattened at the top and bottom so that it was 2.8 cm high and 4.6 cm in diameter. The partial density of free hydrogen for both target materials was about 0.07 g/cm<sup>3</sup>. The target was polarized dynamically in a 25-kG field; the polarization was accomplished by exposing the target to 70-GHz microwaves. A simple 0.4-GHz change in the microwave frequency reversed the polarization. Standard nuclear-magnetic-resonance (NMR) techniques were used to monitor and measure the target polarization, which averaged 80% over the duration of the experiment. The absolute calibration of the NMR system was accomplished by measurements of the thermal-equilibrium (TE) polarization signal at 1 K. The natural polarization at 1 K in a 25-kG  $B$  field is only 0.26%. Because the TE NMR signals were small, the average of 12–20 measurements was used for the NMR calibration. The standard deviation in the TE measurements was 2–3%. Including

TABLE II. Summary of beam characteristics.  $\Delta p$  is the full width at half maximum.

$p_\pi$ (MeV/ $c$ )	$\Delta p/p$ (%)	Rate ( $10^6 \pi^-/\text{sec}$ )	Duty factor (%)	Incident beam angle (degrees)
301	0.25	0.38	6.84	27.4
316	0.25	0.38	6.84	26.6
427	0.30	0.95	10.24	19.5
471	0.40	0.88	10.24	17.7
547	0.50	0.87	10.24	15.3
586	0.65	0.58	6.82	14.3
625	1.00	0.88	10.24	13.4
625	0.70	0.57	6.82	13.4

the errors due to the nonlinearity of the NMR amplifier and the absolute target temperature used in the TE measurements, the systematic uncertainty in the measurement of the target polarization was estimated to be about 4%.

### C. $\gamma$ detectors

$\gamma$ 's were detected in two multicounter detectors, each consisting of 15 counters arranged in a 5 (vertical) by 3 (horizontal) rectangular array, see Fig. 3. Each counter was a  $15 \times 15$ -cm<sup>2</sup>, 25-cm-deep lead-glass block optically isolated from its neighbors by aluminum foil, and it was viewed by a 12.7-cm photomultiplier tube, either an Amperex XP2041 or an RCA 4522. A set of 15 counters was tightly packed inside a  $53 \times 81 \times 43$ -cm<sup>3</sup> aluminum box with interior  $\mu$ -metal shielding, and placed in a 1.3-cm-thick open-ended steel box which helped to shield the photomultiplier tubes from the magnetic field of the polarized-target magnet. The iron box reduced the stray field to 5–10 G at 1.8 m from the target with the magnet at 25 kG. In front of each detector were four double-ended charged-particle veto counters.

The  $\gamma$  counters were calibrated with a 150-MeV electron beam. The lead-glass Cherenkov counters, which were six radiation lengths thick, were better than 90% efficient in detecting  $\gamma$ 's. From a separate study with an electron beam, it was found that electron-initiated electromagnetic showers were contained in a single counter except when electrons entered within 1 cm of the counter's edge. For the purpose of separating the CEX and REX  $\gamma$ 's, the containment of the shower in one counter is important. Single-counter triggers comprised 85% of the total events and two-counter events constituted more than 90% of the multiple-counter triggers. For the double-counter events the signals almost always came from two neighboring counters; it seems likely that these events are due to a  $\gamma$  striking near the edge of a counter with the two adjacent counters sharing the  $\gamma$  energy. Only single- and neighboring two-counter events were processed. For the double-counter events, the proper  $\gamma$  geometry was assigned to the  $\gamma$  counter having the larger pulse-height value. The energy resolution  $\Delta E/E$  of the  $\gamma$  counters was about 25%.

### D. Neutron detectors

Neutrons were detected in two counter arrays, each consisting of 15 counters, see Fig. 3. Each counter was a cylindrical NE110 plastic scintillator 7.6 cm in diameter and 45.7 cm long, viewed at the back by a 5-cm RCA 8575 photomultiplier tube. Shorter counters (19.1 cm) were used for the 301- and 316-MeV/ $c$  measurement at 50° c.m. for better timing resolution. The long counters were about 40% efficient for detecting 150-MeV neutrons and the short counters about 20%. Each set of 15 neutron counters was mounted using two thin aluminum support plates with holes bored out to hold the counters at each end. In front of each 15-counter array was a large double-ended charged-particle veto counter. The neutron counters were calibrated every few days using a <sup>60</sup>Co source by adjusting the counter voltages to set the

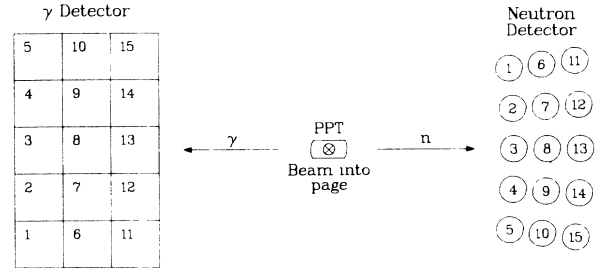


FIG. 3. Neutron- and  $\gamma$ -detector configuration showing the one-to-one neutron-to- $\gamma$ -counter matching for REX.

middle of the Compton edge at 50 mV, which was the neutron-discriminator threshold level.

In order to separate the REX events from the CEX, the neutron counters were arranged such that each counter was matched with one  $\gamma$  counter as dictated by the REX kinematics, see Fig. 3. Because of the one-to-one neutron-to- $\gamma$ -counter arrangement, for each neutron counter the REX events were restricted to one coplanar  $\gamma$  counter, while the CEX events were distributed over the entire  $\gamma$  array.

### E. Event trigger and data acquisition

An event trigger was initiated by a threefold coincidence of a beam, a  $\gamma$ , and a neutron signal. The beam signal was given by a twofold coincidence between the S1 and S2 beam counters. The  $\gamma$  signal was defined by one or more signals in the 15- $\gamma$ -counter array and no signal from the charged-particle veto counters in front. Similarly, a logical OR among the 15 neutron counters of an array in anticoincidence with the charge particle veto counter was used for the neutron signal. Two completely independent sets of electronics were used for each of the two neutron- $\gamma$ -detector pairs. For each coincidence-event trigger, pulse-height and time-of-flight information from all  $\gamma$  and neutron counters were read using analog-to-digital converter (ADC) and time-to-digital converter (TDC) CAMAC modules. The LAMPF standard Q data-acquisition software running on a DEC PDP 11/45 computer with the RSX-11D operating system were used to collect the raw data. Besides the coincidence ADC and TDC data, various scaler information and the target NMR spectrum were collected and recorded for off-line analysis.

## III. DATA ANALYSIS

The left-right asymmetry  $A_N$  is given by the expression

$$A_N = \frac{1}{P_t} \frac{N_\uparrow - N_\downarrow}{N_\uparrow + N_\downarrow - 2B},$$

where  $P_t$  is the target polarization,  $N_\uparrow$  is the yield of good events from the spin-up target,  $N_\downarrow$  is the normalized yield from the spin-down target, and  $B$  is the normalized background yield. The background normalization is discussed in Sec. III A.

The number of good events is obtained upon applica-

tion of cuts on the neutron time-of-flight and  $\gamma$  pulse-height spectra. The very same set of cuts are applied to the spin-up, spin-down, and the background target data, and the resulting yields are then used to calculate the left-right asymmetry. The asymmetries were normally calculated for each succeeding step during the analysis to determine the effectiveness and consistency of the cuts applied.

The clearest experimental signal for CEX is a sharp peak in the neutron time-of-flight (TOF) spectrum, see Fig. 4(a), this peak is marked by an  $n$  in the figure. The  $\gamma$  peak in this histogram is due to the prompt events which have the TOF of a photon. All our timing measurements were initiated by the triggering  $\gamma$  counter, so the neutron TOF is the time difference between the  $\gamma$  trigger and the neutral particle detected in the neutron counter. Since the CEX  $\gamma$ 's associated with each neutron counter can go to any of the 15  $\gamma$  counters, the timing alignment of the  $\gamma$  counters is particularly important. The  $\gamma$  counters were aligned in time to 1–2 nsecs during data acquisition. In the off-line analysis, the  $\gamma$  counter starts were aligned to 0.2 nsec in the software to give the sharp CEX peak, see Fig. 4(a). The  $\gamma$  timing alignment procedure used the S1·S2 beam counter timing signal, which relates the TOF of the  $\gamma$  from the target to the triggering  $\gamma$  counter.

The prominent neutron peak in Fig. 4 comes mainly from CEX neutrons. Except at 301 and 316 MeV/c where separate REX and CEX peaks are seen, the TOF difference between the REX and CEX neutrons is less than 1 nsec and the small REX neutron peak is hidden under the CEX peak. The width of the CEX neutron TOF peak ranged from 3 nsec for 625 MeV/c and 4 nsecs for 427 MeV/c to 16 nsec for 301 MeV/c at  $\bar{\theta}_{\pi^0} = 32.5^\circ$ . The broad width at 301 MeV/c is due to the  $4^\circ$  spread in the scattering angle, which gives the CEX neutron a velocity ( $v/c$ ) range of 0.12–0.15; for the 235-cm flight path to the neutron counter this causes a TOF difference of 13 nsec.

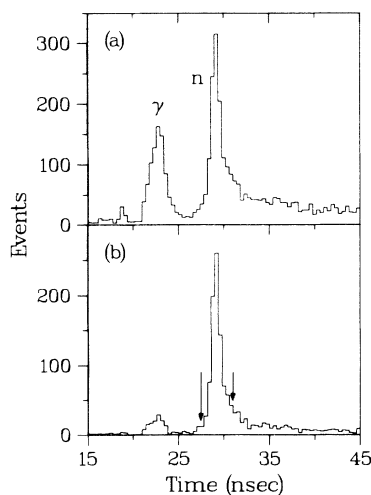


FIG. 4. Neutron TOF spectrum, (a) before, and (b) after the  $\gamma$  pulse-height cut. The REX and the CEX events are extracted using a tight cut about the sharp REX-CEX composite peak indicated by the arrows in (b).

The neutron TOF spectrum was “cleaned” by applying a cut on the  $\gamma$  pulse-height spectrum, which is dominated by low-energy  $\gamma$ 's from the background reactions. A typical  $\gamma$  ADC spectrum is shown in Fig. 5(a) for the case where the REX  $\gamma$  laboratory energy is 300 MeV and the CEX  $\gamma$ 's are between 100–300 MeV. The  $\gamma$  pulse-height cut was very effective in eliminating much of the background, as can be seen by comparing Fig. 4(a) with Fig. 4(b) in which a  $\gamma$  pulse-height cut corresponding to 10 units on the scale of Fig. 5(a) has been applied; this particular cut removed over 60% of the background events in the CEX peak region. The magnitude of the  $\gamma$  pulse-height cut was decided by comparing the  $\gamma$  spectrum for all events and a subset of CEX enhanced events, obtained by applying cuts about the CEX neutron TOF peak. The CEX  $\gamma$  peak shown in Fig. 5(b) is broad, due to the fact that the CEX  $\gamma$  energy depends on the opening angle with respect to the parent  $\pi^0$ , and the  $\gamma$ -counter energy resolution is about 25%. Knowing the precise value of the  $\gamma$  pulse-height cut is irrelevant because the asymmetry is a relative measurement between spin-up and spin-down scattering. However, it is important that the experimental conditions remain the same, which was ensured by collecting the data in spin pairs by reversing the target polarization every 8 hours to minimize any long term drifts in the apparatus. A pulse-height cut of about 180 MeV is typically applied to keep about 70% of the events from the CEX peak and reject the rest along with the large number of low-energy background events. The asymmetries were calculated for three different pulse-height cuts and they were found to be consistent. The error in the asymmetry is the largest when no  $\gamma$  pulse-height cut is applied because of the sizable background.

After the  $\gamma$  pulse-height cut, the CEX events were obtained from the neutron TOF spectra with tight cuts about the CEX neutron peak. The selected events are mostly CEX events with a small number of REX events,

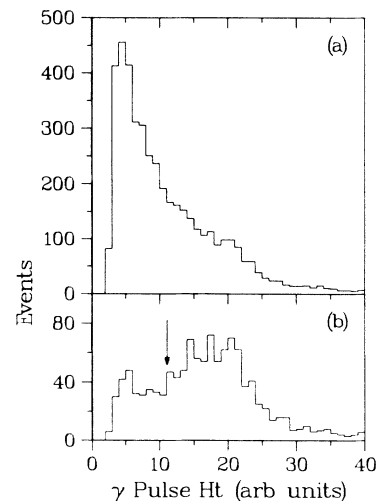


FIG. 5. Typical  $\gamma$  pulse-height spectrum at  $p_\pi = 625$  MeV/c and  $\bar{\theta}_\pi = 75^\circ$ , (a) all events, (b) a subset of CEX-enhanced events obtained by requiring a TOF condition on the neutron. The arrow indicates the lower limit of the  $\gamma$  pulse-height cut.

TABLE III. Dependence of the 586-MeV/*c* CEX asymmetry values on three different neutron TOF cuts.

$\bar{\theta}_{\pi^0}$ (deg)	$A_N \pm \sigma_{A_N}$	Number of events			TOF cut
		CEX ↑	CEX ↓	Background	
84.3	$0.862 \pm 0.024$	3327	598	570	4 nsec wide
	$0.876 \pm 0.023$	3148	540	472	3 nsec
	$0.872 \pm 0.026$	2334	404	340	2 nsec
88.0	$0.785 \pm 0.026$	2802	627	574	4 nsec
	$0.792 \pm 0.025$	2684	595	461	3 nsec
	$0.804 \pm 0.027$	2183	467	332	2 nsec
91.5	$0.675 \pm 0.024$	2917	861	639	4 nsec
	$0.677 \pm 0.023$	2802	823	475	3 nsec
	$0.665 \pm 0.026$	2135	647	324	2 nsec

which could not be separated because of insufficient TOF flight difference between the two reactions. Therefore, in calculating the CEX asymmetries one must use extra care not to include any REX events especially since the CEX and the REX asymmetries can differ in sign. With our experimental arrangement of the counters, the coplanar neutron- $\gamma$ -counter pairs contain more than 80% of all REX events with the rest distributed over the adjacent (neighboring)  $\gamma$  counters, see Fig. 6. In calculating the CEX asymmetry values, only the events from the noncoplanar and the nonadjacent counters were used.

The dependence of the asymmetry values on three different neutron TOF cuts is illustrated in Table III. Because the asymmetry is a relative measurement between the spin-up and the spin-down target, the asymmetry should be independent of any specific sets of cuts applied to the data. Three sets of asymmetry values were calculated for different widths of the neutron TOF window. All three widths gave consistent results as shown in Table III.

#### A. Background

Quasifree charge-exchange scattering on the nonhydrogenic parts of the polarized target, such as carbon and oxygen atoms in the target material, the target cell, and the steel container, and the  $^3\text{He}$  refrigerant, contributed to the background. Most of the background events were removed by the neutron TOF and the  $\gamma$  pulse-height cuts. The remaining background events were subtracted using the “dummy”-target data obtained in separate runs with teflon ( $\text{C}_2\text{F}_4$ ) beads replacing the ethylene glycol ( $\text{C}_2\text{H}_6\text{O}_2$ ) target beads. For the 301- and 316-MeV/*c* data, 1,2-propanediol ( $\text{C}_3\text{H}_8\text{O}_2$ ) was used as the polarized proton target and carbon beads were used as the background target.

The solid curve in Fig. 7(a) is a neutron TOF spectrum using the teflon target, while the bars are data obtained with the polarized target. The composite REX and CEX peak sits atop a broad background which is removed by subtracting the normalized TOF spectrum taken with the background target; after the background subtraction, only the REX and CEX events remain as in Fig. 7(b).

In our asymmetry measurement, only the relative normalizations between the spin-up, the spin-down, and the background runs are needed. For convenience, the spin-down and the background runs are normalized to the spin-up runs. The spin-down-to-spin-up normalization is given by the ratio of the number of incident-beam particles obtained from the S1·S2 beam monitor in the spin-up and spin-down runs.

The background normalization was accomplished by comparing the height of the neutron TOF spectra from the background target runs to the polarized target runs in the region of the broad background away from the CEX peak, such that the broad background would be exactly canceled by the normalized spectra from the background runs. By normalizing with respect to the neutron TOF spectra, many factors such as differences in target density and composition between the background and the polarized target runs are automatically included, since the TOF spectra reflect the actual experimental conditions of

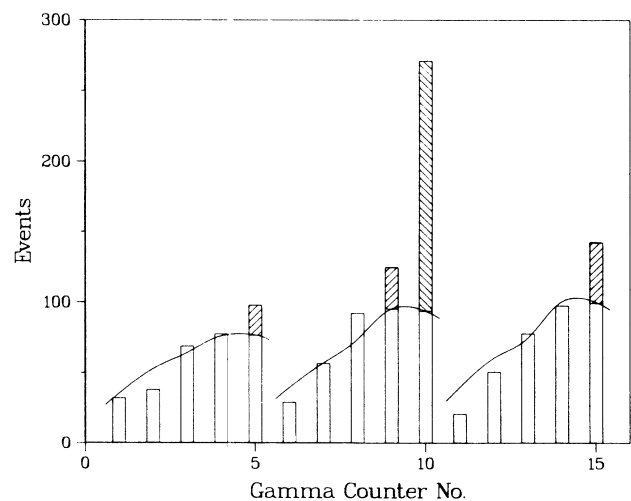


FIG. 6. A sample event distribution in the 15  $\gamma$  counters for one (counter 10) of the neutron counters. The solid curve is the Monte Carlo-generated CEX distribution normalized to fit the data. The shaded boxes represent the REX events above the CEX events in the coplanar (10) and the adjacent counters, 5, 9, and 15.

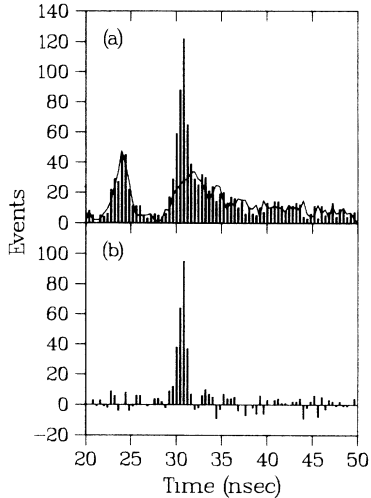


FIG. 7. Neutron TOF spectra. (a) Polarized-target data (bar graph) and the “dummy”-background target (solid curve). (b) Difference between the polarized target and the normalized background data. This is a bin-by-bin subtraction of the bar and solid graphs of Fig. (a).

the runs. The subtracted neutron TOF spectrum obtained by a bin-by-bin subtraction of a normalized background target spectrum from a polarized target spectrum is shown in Fig. 7(b). As one can see from the figure, the off-time region to the right of the CEX peak is flat and the number of events fluctuates about zero, indicating that the background was correctly subtracted and that the peak contains only REX and CEX events.

Applying the off-time normalization method to all neutron counters and then averaging over the individual counters results in about  $\pm 5\%$  uncertainty in the background normalization at each beam momentum. The error in the CEX asymmetries due to the 5% background normalization uncertainty was found to be less than the magnitude of the statistical error as demonstrated in Table IV.

## B. Uncertainties

The statistical uncertainty in the asymmetry is calculated using the standard propagation of errors method. The uncertainty in  $A_N$  is given by

$$\sigma_{A_N} = 2P_t \frac{A_N^2}{(N_\uparrow - N_\downarrow)^2} [(N_\downarrow - B)^2 \sigma_{N_\uparrow}^2 + (N_\uparrow - B)^2 \sigma_{N_\downarrow}^2 + (N_\uparrow - N_\downarrow)^2 \sigma_B^2]^{1/2}.$$

Using Poisson statistics, the variances of  $N_\uparrow$ ,  $N_\downarrow$ , and  $B$  are

$$\sigma_{N_\uparrow}^2 = N_\uparrow, \quad \sigma_{N_\downarrow}^2 = N_\downarrow,$$

and

$$\sigma_B^2 = B.$$

Including the systematic uncertainty from the target polarization, the total uncertainty in  $A_N$  is

$$\sigma_{A_N}^{\text{tot}} = \left[ \sigma_{A_N}^2 + A_N^2 \left( \frac{\sigma_{P_t}}{P_t} \right)^2 \right]^{1/2}.$$

Because the 4% uncertainty in the polarization scales the asymmetry values by  $(1 \pm \Delta P_t / P_t)$ , only the statistical errors are given.

## IV. RESULTS AND DISCUSSION

The results for the left-right asymmetry  $A_N$  in  $\pi^-p \rightarrow \pi^0n$  at  $p_\pi = 301, 316, 427, 471, 547, 586,$  and  $625$  MeV/c are listed in Table V. The errors given in the table are the combination of the statistical uncertainty and the 5% uncertainty in the background normalization, but without the 4% systematic uncertainty in the absolute value of the target polarization.

Our CEX data are compared with the predictions of recent partial-wave analyses by the Karlsruhe-Helsinki<sup>10</sup> (KH), the Carnegie Mellon University-Lawrence Berkeley Laboratory<sup>11</sup> (CL), and the Virginia Polytechnic Institute<sup>12</sup> (VPI) group in Figs. 8–10. None of the aforemen-

TABLE IV. Effect on the 547-MeV/c CEX asymmetry values from varying the background normalization by  $\pm 5\%$ .

$\bar{\theta}_{\pi^0}$ (deg)	$A_N \pm \sigma_{A_N}$	CEX $\uparrow$	Number of events			Background normalization change
			CEX $\downarrow$	Background		
83.8	$0.894 \pm 0.019$	3914	684	515	-5%	
	$0.908 \pm 0.020$	3878	648	551	0%	
	$0.922 \pm 0.021$	3842	612	587	+5%	
87.7	$0.866 \pm 0.019$	3854	730	522	-5%	
	$0.880 \pm 0.020$	3818	695	558	0%	
	$0.894 \pm 0.021$	3781	658	595	+5%	
91.6	$0.718 \pm 0.019$	3744	1045	501	-5%	
	$0.728 \pm 0.019$	3709	1010	536	0%	
	$0.739 \pm 0.020$	3674	975	571	+5%	

TABLE V. Results for the left-right-asymmetry parameter  $A_N$  in  $\pi^- p \rightarrow \pi^0 n$  measured with a transversely polarized target.

$p_\pi$ (MeV/c)	$\bar{\theta}_{\pi^0}$ (deg)	$\cos\bar{\theta}_{\pi^0}$	$A_N$	$\sigma_{A_N}$	$p_\pi$ (MeV/c)	$\bar{\theta}_{\pi^0}$ (deg)	$\cos\bar{\theta}_{\pi^0}$	$A_N$	$\sigma_{A_N}$
301	32.5	0.84	0.251	0.029	316	30.8	0.86	0.247	0.025
	38.8	0.78	0.302	0.025		37.1	0.80	0.257	0.022
	81.4	0.15	0.678	0.049		79.6	0.18	0.675	0.038
	85.3	0.08	0.730	0.042		83.6	0.11	0.702	0.036
	89.3	0.01	0.686	0.040		87.6	0.04	0.684	0.032
427	82.7	0.13	0.922	0.024	471	83.0	0.12	1.010	0.027
	86.7	0.06	0.909	0.023		86.9	0.05	0.959	0.028
	90.5	-0.01	0.892	0.023		90.8	-0.01	0.904	0.026
	103.5	-0.23	0.313	0.035		104.1	-0.24	0.339	0.039
	107.4	-0.30	0.138	0.034		107.9	-0.31	0.098	0.043
	111.1	-0.36	-0.033	0.028	111.6	-0.37	-0.071	0.036	
547	83.8	0.11	0.908	0.021	586	84.3	0.10	0.876	0.024
	87.7	0.04	0.880	0.021		88.0	0.03	0.792	0.026
	91.6	-0.03	0.728	0.020		91.5	-0.03	0.677	0.024
	104.4	-0.25	0.334	0.028		104.7	-0.25	0.289	0.034
	108.3	-0.31	0.239	0.031		108.5	-0.32	0.313	0.038
	112.0	-0.37	0.208	0.027	112.3	-0.38	0.249	0.032	
625	68.9	0.36	1.056	0.020	625	99.7	-0.17	0.390	0.032
	72.5	0.30	1.015	0.020		103.6	-0.24	0.298	0.033
	75.9	0.24	0.998	0.020		107.4	-0.30	0.298	0.032
	84.5	0.10	0.778	0.024		115.4	-0.43	0.344	0.045
	88.2	0.03	0.696	0.025		118.9	-0.48	0.499	0.058
	91.8	-0.03	0.589	0.023	122.3	-0.53	0.512	0.052	

tioned PWAs include our results in their data base. To make a numerical comparison between our data and the PWAs, we calculated the quantity

$$\chi^2 = \frac{1}{n} \sum \frac{(A_N - A_N^{\text{PWA}})^2}{\sigma_{A_N}^2},$$

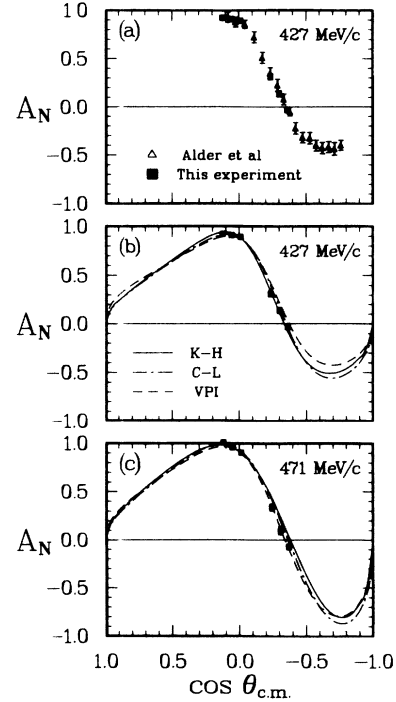
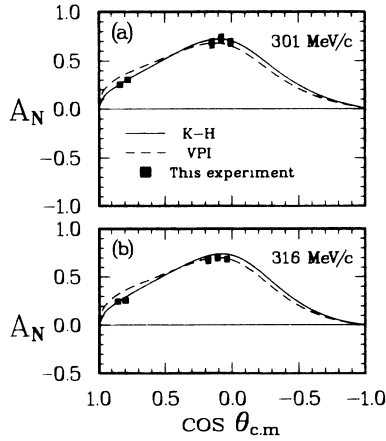
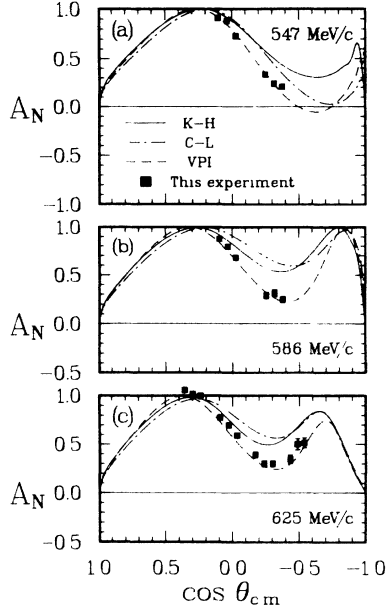


FIG. 8. Analyzing power  $A_N$  in  $\pi^- p \rightarrow \pi^0 n$  measured with a transversely polarized target at  $p_\pi = 301$  and  $316$  MeV/c. The solid line is the KH  $\pi N$  PWA prediction (Ref. 10), and the dash line is VPI (Ref. 12).

FIG. 9. Same as Fig. 8 at  $p_\pi = 427$  and  $471$  MeV/c. The dotted-dash line is the CL PWA prediction (Ref. 11). The open triangles in (a) are the data of Alder *et al.* (Ref. 21).

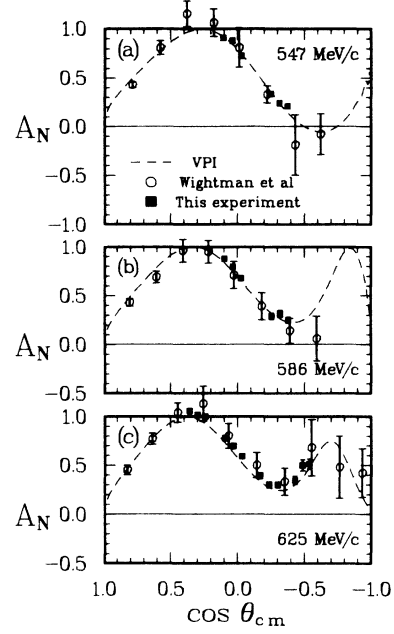
FIG. 10. Same as Fig. 8 at  $p_\pi = 547, 586,$  and  $625$  MeV/c.

where  $A_N^{\text{PWA}}$  is the asymmetry predicted from the partial-wave analysis. The results which are given in Table VI are calculated with and without the  $\pm 4\%$  systematic uncertainty in  $A_N$ .

The experiment can be divided into three energy regions.

(a) The measurements at 301 and 316 MeV/c cover the area just around the peak of the  $\Delta(1232)$  resonance. The asymmetry curves predicted by KH and VPI have a similar overall shape, see Figs. 8(a) and 8(b). Both the KH and the VPI PWAs are in good agreement with our results, our data show a slight overall preference for KH over VPI due to the better agreement with KH at the forward angle.

(b) The measurements at 427 and 471 MeV/c are in a region where there is no  $\pi N$  resonance. The asymmetry curves predicted by KH, CL, and VPI are very similar, see Figs. 9(b) and 9(c). The asymmetry curves are characterized by large asymmetries approaching 1 near  $\cos\theta = 0.1$ , and a subsequent rapid decrease which leads to a negative peak at  $\cos\theta = -0.7$ . Our data show a very slight preference for KH and CL over VPI at 427 MeV/c; the VPI predictions give slightly larger  $A_N$  than our data

FIG. 11. Comparison of our  $A_N$  results with the data of Wightman *et al.* (Ref. 22).

at  $\cos\theta$  from  $-0.2$  to  $-0.4$ . Our data at 427 MeV/c are compared with the results of Alder *et al.*,<sup>21</sup> see Fig. 9(a), and the agreement is excellent. At 471 MeV/c, our data show a slight preference for VPI and CL over KH, where the KH predictions at angles  $-0.2 > \cos\theta > -0.4$  give slightly larger asymmetry values than our results.

(c) The region of greatest interest is from 547 to 625 MeV/c. As shown in Figs. 10(a)–10(c), the three PWA predictions agree well with each other in the forward angles, but diverge badly in the backward angles. Our data overwhelmingly favor VPI and their lower minimum in the backward angles. Our results are compared with the recent data of Wightman *et al.*,<sup>22</sup> see Figs. 11(a)–11(c). Within their larger errors there is good agreement with our data.

Our CEX asymmetry results may be presented as transversity cross sections by combining the asymmetries with the CEX differential cross sections to give

$$d\Sigma_{\uparrow} = d\sigma(1 + A_N) \quad \text{and} \quad d\Sigma_{\downarrow} = d\sigma(1 - A_N).$$

TABLE VI. Numerical comparison of  $\chi^2$  of our data with various PWA predictions. The three columns indicate the effect of the  $\pm 4\%$  uncertainty in the absolute polarization of the target.

$p_\pi$ (MeV/c)	KH			CL			VPI		
	-4%	0%	+4%	-4%	0%	+4%	-4%	0%	+4%
301	0.3	0.2	0.7				3.7	3.7	4.3
316	0.5	1.5	3.4				5.3	6.4	8.2
427	1.5	0.9	2.8	3.1	1.6	2.5	7.3	4.8	4.9
471	6.3	4.8	5.4	3.1	2.1	3.1	3.4	0.8	0.5
547	38	46	55	26	34	44	3.5	1.5	2.3
586	31	36	43	66	76	87	5.6	2.2	0.7
625	17	17	19	35	35	39	12	5.4	1.7

The transversity-up and transversity-down cross sections are the cross sections from a fully polarized target with the polarization direction up and down. The transversity cross sections provide a sensitive test of isospin invariance via triangle inequalities on  $\pi^\pm p$  elastic and  $\pi^- p$  charge-exchange cross sections. Using the CEX differential-cross-section data of Borcherding<sup>23</sup> our 547- and 625-MeV/c results have been presented in Ref. 22. A similar test at 471 MeV/c was made and no evidence for isospin violation was found.

## V. SUMMARY AND CONCLUSION

We have measured  $A_N(\pi^- p \rightarrow \pi^0 n)$  from 301 to 625 MeV/c, at a limited number of angles but with high statistical accuracy. Our  $A_N(\text{CEX})$  results agree well with the PWA predictions by the VPI group at all seven incident beam momenta. It is easy to blame the  $P_{11}$  wave for the disagreement among the PWAs because of the different values quoted for the  $P_{11}$  parameters. It was pointed out by Hohler<sup>24</sup> that in the energy region of this experiment the largest difference is in the values for the  $S_{11}$  wave. This is illustrated in Fig. 12, which gives the amplitude of the  $S_{11}$  and  $P_{11}$  as obtained by the PWAs. As Fig. 12(b) shows, the three PWA groups obtain very similar values for the  $P_{11}$  amplitude up to  $W=1600$  MeV. The conflicting values for the mass, width, and pole position (or positions) of the Roper resonance of the three PWAs are due to the differences in the higher-energy contribution,  $W > 1600$  MeV, and different theoretical analyses. Further experimental work, including the inelastic reactions such as  $\pi^- p \rightarrow \gamma n$ ,  $\pi^- p \rightarrow \pi\pi N$ , and  $\pi^- p \rightarrow \eta n$ , are needed to understand the detailed structures of the  $P_{11}$  resonance. Since the characteristics of the  $\pi N$  resonances given in the Particle Data Group tables come from the KH and CL PWAs, the poor agreement of our  $A_N$  data in the 500–600-MeV/c region implies some uncertainty in the listed  $S_{11}$

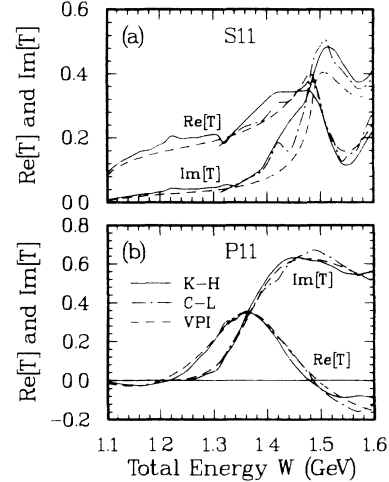


FIG. 12. PWA predictions (Refs. 10–12) for  $P_{11}$  and  $S_{11}$  scattering amplitudes.

and  $P_{11}$  parameters and presumably in the larger-mass resonances as well.

## ACKNOWLEDGMENTS

We gratefully acknowledge the loan of the polarized target by J. E. Simmons and the Los Alamos  $P$ -Division. Also we thank V. Highland of Temple University for the loan of the  $\gamma$  counters. We appreciate the efforts of R. Damjanovich and the MP-8 crew in mounting the experiment, and the help given by J. Jarmer and J. Vaninetti with the target. This work was supported in part by the U.S. Department of Energy, and the National Science Foundation. W.J.B. acknowledges the George Washington University Committee on Research, and M. E. S. the Research Council at Abilene Christian University.

\*Current address: Cyclotron Institute, Texas A&M University, College Station, TX 77843.

†Current address: Physics Department, University of Bonn, West Germany.

‡Current address: Lawrence Livermore National Laboratory, Livermore, CA 94550.

§Current address: Los Alamos National Laboratory, Los Alamos, NM 87545.

<sup>1</sup>Particle Data Group, G. P. Yost *et al.*, Phys. Lett. B **204**, 366 (1988).

<sup>2</sup>N. Isgur and G. Karl, Phys. Rev. D **18**, 4187 (1978); **19**, 2653 (1979).

<sup>3</sup>K. C. Bowler and A. J. G. Hey, Phys. Lett. **69B**, 469 (1977).

<sup>4</sup>T. A. DeGrand and C. Rebbi, Phys. Rev. D **17**, 2358 (1978).

<sup>5</sup>F. E. Close and R. R. Horgan, Nucl. Phys. **B164**, 413 (1980).

<sup>6</sup>E. Umland, I. Duck, and W. von Witsch, Phys. Rev. D **27**, 2678 (1983).

<sup>7</sup>J. Carlson, J. B. Kogut, and V. R. Pandharipande, Phys. Rev. D **28**, 2807 (1983).

<sup>8</sup>M. P. Mattis and M. Karliner, Phys. Rev. D **31**, 2833 (1985);

M. Karliner and M. P. Mattis, *ibid.* **34**, 1991 (1986).

<sup>9</sup>A. Hayashi, G. Eckart, G. Holzwarth, and H. Walliser, Phys. Lett. **147B**, 5 (1984); G. Eckart, A. Hayashi, and G. Holzwarth, Nucl. Phys. **A448**, 732 (1986).

<sup>10</sup>G. Hohler, F. Kaiser, R. Koch, and E. Pietarinen, *Handbook of Pion-Nucleon Scattering* (Karlsruhe, Germany, 1979); also R. Koch and E. Pietarinen, Nucl. Phys. **A336**, 331 (1980).

<sup>11</sup>R. E. Cutkosky, C. P. Forsyth, R. E. Hendrick, and R. L. Kelly, Phys. Rev. D **20**, 2839 (1979).

<sup>12</sup>R. A. Arndt, L. D. Roper, and J. Ford, Phys. Rev. D **32**, 1085 (1985).

<sup>13</sup>G. J. Kim, S. D. Adrian, J. Arends, W. J. Briscoe, J. Engelage, B. M. K. Nefkens, M. E. Sadler, C. J. Seftor, D. I. Sober, M. Taragin, and H. J. Ziock, Phys. Lett. B **219**, 62 (1989).

<sup>14</sup>R. E. Cutkosky, in *Physics with Light Mesons and the Second International Workshop on Pion-Nucleus Physics*, proceedings of the Workshops, Los Alamos, New Mexico, 1987, edited by W. R. Gibbs and B. M. K. Nefkens (LANL, Los Alamos, 1988).

<sup>15</sup>T. Barnes and F. E. Close, Phys. Lett. **116B**, 365 (1982); T.

- Barnes and F. E. Close, *ibid.* **123B**, 89 (1983).
- <sup>16</sup>M. Chanowitz and S. Sharpe, Nucl. Phys. **B222**, 211 (1983).
- <sup>17</sup>B. Blankleider and G. E. Walker, Phys. Lett. **152B**, 291 (1985).
- <sup>18</sup>D. Strottman, Phys. Rev. D **18**, 2716 (1978).
- <sup>19</sup>G. J. Kim, S. D. Adrian, J. Arends, W. J. Briscoe, A. D. Eichon, J. Engelage, S. Graessle, B. M. K. Nefkens, Y. Ohashi, M. E. Sadler, C. J. Seftor, D. I. Sober, M. Taragin, and H. J. Ziock, Phys. Rev. Lett. **56**, 1779 (1986).
- <sup>20</sup>D. Roeder and R. J. Macek, Los Alamos National Laboratory Report No. LA-7268-pr, 1977 (unpublished); and W. J. Briscoe, D. H. Fitzgerald, B. M. K. Nefkens, and M. E. Sadler, Nucl. Instrum. Methods **197**, 277 (1982).
- <sup>21</sup>J. C. Alder, C. Joseph, J. P. Perroud, M. T. Tran, G. H. Eaton, R. Frosh, H. Hirschmann, S. Mango, J. W. McCulloch, P. Shrager, G. Strassner, P. Truol, P. Weymouth, and P. Wiederkehr, Phys. Rev. D **27**, 1040 (1983).
- <sup>22</sup>J. A. Wightman, A. D. Eichon, G. J. Kim, A. Mokhtari, B. M. K. Nefkens, W. J. Briscoe, D. H. Fitzgerald, and M. E. Sadler, Phys. Rev. D **38**, 3365 (1988).
- <sup>23</sup>F. O. Borcharding, Ph.D. thesis, University of California at Los Angeles 1982.
- <sup>24</sup>G. Hohler (private communication).